Letter

Proximity-effect-induced superconductivity in a van der Waals heterostructure consisting of a magnetic topological insulator and a conventional superconductor

Peng Dong,[1,*] Xiaofei Hou,[1,*] Jiadian He,[1] Yiwen Zhang,[1] Yifan Ding,[1] Xiaohui Zeng,[1] Jinghui Wang,[1] Yueshen Wu,[1] Kenji Watanabe,[2] Takashi Taniguchi,[3] Wei Xia,[1,†] Yanfeng Guo,[1] Yulin Chen,[1,4] Xiang Zhou,[1,‡] Wei Li,[5,§] and Jun Li[1,‖]

[1]*ShanghaiTech Laboratory for Topological Physics & School of Physical Science and Technology, ShanghaiTech University, Shanghai 201210, China*

[2]*Research Center for Functional Materials, National Institute for Materials Science, Tsukuba 305-0044, Japan*

[3]*International Center for Materials Nanoarchitectonics, National Institute for Materials Science, Tsukuba 305-0044, Japan*

[4]*Department of Physics, Clarendon Laboratory, University of Oxford, Oxford OX1 3PU, United Kingdom*

[5]*State Key Laboratory of Surface Physics and Department of Physics, Fudan University, Shanghai 200433, China*

(Received 29 October 2023; revised 12 March 2024; accepted 21 March 2024; published 8 April 2024)

Nontrivial topological superconductivity has received enormous attention due to its potential applications in topological quantum computing. The intrinsic issue concerning the correlation between a topological insulator and a superconductor is, however, still widely open. Here, we systemically report an emergent superconductivity in a cross junction composed of a magnetic topological insulator $MnBi_2Te_4$ and a conventional superconductor $NbSe_2$. Remarkably, the interface indicates the existence of a reduced superconductivity at the surface of $NbSe_2$ and a proximity-effect-induced superconductivity at the surface of $MnBi_2Te_4$. Furthermore, the in-plane angular-dependent magnetoresistance measurements unveil distinctive features indicative of unconventional pairing symmetry in these superconducting gaps. Our findings extend our views and ideas of topological superconductivity in the superconducting heterostructures with time-reversal symmetry breaking, offering an exciting opportunity to elucidate the cooperative effects on the surface state of a topological insulator aligning a superconductor.

DOI: 10.1103/PhysRevB.109.L140503

Topological superconductors (TSCs), which can host Majorana quasiparticles [1,2], are generally considered as a promising path to obey non-Abelian statistics and encode and manipulate quantum information in a topologically protected manner [3,4]. Commonly, the superconductivity gap symmetry of TSC behaves in a nontrivial topological nature, and the pair potential of Cooper pairs exhibits an anisotropic orbital symmetry, such as a chiral *p*-wave superconductivity [5]. Up to now, the most persuasive way to achieve TSC is through the conventional *s*-superconductor proximate to a topological insulator (TI) [6–12]. Due to the inevitable degradation of superconducting wave function into the TIs in the presence of the interfacial electronic states [13–16], interface control is challenging for topological superconducting heterostructure engineering.

Recently, the van der Waals magnet $MnBi_2Te_4$ (MBT) has attracted great attention owing to the existence of the long-range magnetic order in the nontrivial topological phase [17–21]. MBT crystallizes alternatively stacking, topological insulating Bi_2Te_3 layers and metallic MnTe layers. As a consequence, the bulk MBT behaves as a Weyl semimetal [20]. In addition, MBT is an A-type antiferromagnet (AFM) in which the Mn^{2+} ions are ferromagnetically ordered within a single layer (SL) while antiferromagnetically coupled between layers when the temperature is lower than the Neél temperature. Therefore, of particular interest is that when the topological MBT flake with time-reversal symmetry breaking is proximate to a conventional superconductor (SC), the heterointerface will provide an ideal path to understanding the emergence of rich topological superconducting phenomena. Historically, it has been proposed in theory that a heterostructure comprised of MBT and a conventional *s*-wave SC probably induces a TSC associated with chiral Majorana edge modes. In experiments, the superconducting thin films of NbN have been grown on MBT [22,23], and a proximity-effect-induced superconductivity gap of about 0.1 meV has been observed. More interestingly, a clear Coulomb blockade oscillation has been perceived. Nevertheless, the understanding of the surface state of MBT in proximity to a superconductor remains a complex and challenging area of research, and many questions still lack comprehensive answers.

In this work we fabricated MBT/$NbSe_2$ heterostructures by stacking the single-crystalline MBT and $NbSe_2$ flakes. We simultaneously studied the transport properties of the $NbSe_2$, the MBT, the whole heterostructure, and the heterointerface by choosing different electrodes on the heterostructures. Intriguingly, three superconducting gaps have been perceived through the measurements on the heterostructures, including the intrinsic $NbSe_2$, the reduced superconductivity at the

*These authors contributed equally to this work.
†xiawei2@shanghaitech.edu.cn
‡zhouxiang@shanghaitech.edu.cn
§w_li@fudan.edu.cn
‖lijun3@shanghaitech.edu.cn

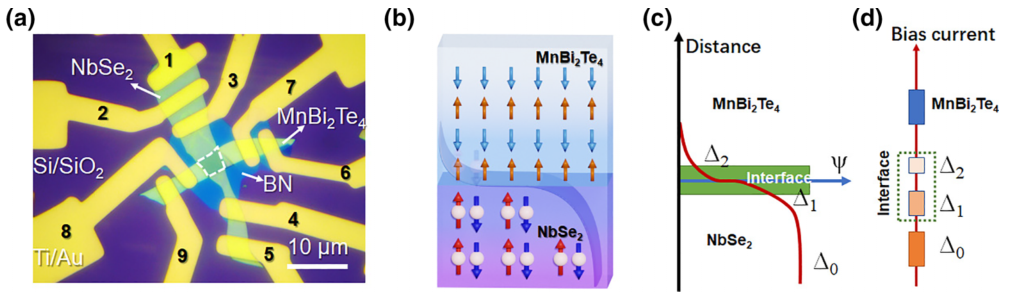

FIG. 1. Sample geometry and the interface of MBT/$NbSe_2$. (a) The optical microscopic image of the MBT/$NbSe_2$ structure. The bottom *h*-BN(20 nm) provides an atomic flat substrate, and MBT (40 nm) and $NbSe_2$ (30 nm) flakes are stacked as a heterostructure, in which the junction area is labeled by a white dash line. Nine electrodes marked from 1 to 9 are connected in different configurations of current flowing and voltage measurement for comparison of electrical properties of the pristine $NbSe_2$ (current 1-5, voltage 2-3), MBT (6-9, 7-8), the whole heterostructure (1-6, 3-8), and the interface (1-6, 5-9) channels. (b) Schematic images of MBT/$NbSe_2$ heterostructure. MBT reveals an antiferromagnetic order along the out-of-plane, while electrons in $NbSe_2$ demonstrate Cooper pairs with opposite spin directions in the superconducting state. (c) Schematic image of the degradation of the superconducting wave function (ψ) along the distance from $NbSe_2$. Here, Δ_0, Δ_1, and Δ_2 correspond to the superconductivity gaps of the intrinsic $NbSe_2$, the surface superconductivity of $NbSe_2$, and the proximity-effect-induced superconductivity at the MBT surface. (d) The equivalent circuit of the junction.

surface of $NbSe_2$, and the proximity-effect-induced superconductivity at the surface of MBT.

Figure 1(a) shows the optical microscopic image and the schematic diagram of the MBT/$NbSe_2$ cross junction, where the superconducting $NbSe_2$ flake (~30 nm in thickness) was stacked on top of the magnetic topological MBT flake (~40 nm), configuring a crosslike junction, and a 20-nm-thick insulating *h*-BN was laid on the bottom of the heterostructure as a substrate. The electrodes on MBT and $NbSe_2$ flakes can be selected in various channels to reveal the electronic properties of the $NbSe_2$, the MBT, the whole heterostructure, and its heterointerface.

Considering the interface between the MBT and $NbSe_2$, as given in Fig. 1(b), MBT reveals a ferromagnetic order along the out-of-plane, while electrons in $NbSe_2$ are condensed into Cooper pairs which behave as a singlet superconducting state (↑↓-↓↑) below the critical temperature (T_c). As has been demonstrated before [24], when the distance from $NbSe_2$ increases, its superconducting gap Δ_0 will gradually degenerate and form a reduced superconductivity gap Δ_1 at the interface, as illustrated in Fig. 1(c). Notably, the gap Δ_1 strongly depends on the electron state of the non-SC side. Once the non-SC side is a normal metal, the superconducting wave function from the $NbSe_2$ can flow into the metal within a distance less than the coherence length $\xi_N = \sqrt{\hbar D/k_B T}$, where D is the diffusion coefficient [24], while for a magnetic material, the superconductivity coherence length (ξ_M) turns into $\xi_M = \sqrt{\hbar D_M/k_B T_M}$, where T_M is the magnetic transition temperature. Meanwhile, the superconducting wave function decays exponentially, $\Delta_M = \exp(D_M \xi_M)$, due to the existence of the exchange splitting from the spin-spin interaction, resulting in a restricted superconducting gap function (Δ_2). Since the exchange splitting is absent in an AFM, the superconductivity coherence length should be comparable to that of normal metal. However, due to the A-type AFM magnetic structure of MBT, it is essential to take into account the ferromagnetic coupling when considering the interface between MBT and $NbSe_2$.

As illustrated in Figs. 2(a), 2(e), 2(i), and 2(m), we can evaluate the electronic properties of $NbSe_2$, MBT, the whole heterostructure, and the interface by choosing electrodes on the MBT and $NbSe_2$ flakes [see Fig. 1(a)]. The detailed analysis is introduced in the Supplemental Material [25]. For the pristine $NbSe_2$, the temperature- and magnetic-field-dependent resistances are shown in Figs. 2(b) and 2(c), respectively, indicating the intrinsic superconductivity of $NbSe_2$. Specifically, a superconducting transition temperature (T_c) of 7 K and a critical field (B_c) of 3 T at 1.8 K were observed. Moreover, the critical current of $NbSe_2$ is about 1.8 mA at 1.8 K, as shown in Fig. 2(d). According to the electron-phonon coupling strength in BCS model $2\Delta_0 = 3.52 k_B T_c$, we can estimate the superconducting gap of the pristine $NbSe_2$ to be 1.2 meV at $T = 0$ K, which is consistent with previous reports [26].

The transport properties of MBT are consistent with previous results [19,27–29], where the Neél temperature (T_N) is 23.7 K [see Fig. 2(f)], and the spin-flop critical field (B_c^{MBT}) is ~3.34 T [see Fig. 2(g)]. It seems that the B_c^{MBT} is comparable to that of the B_c of $NbSe_2$ (~3 T). Despite this, we can easily distinguish the contribution of MBT or $NbSe_2$, because they induce opposite modifications on the magnetoresistance. Namely, MBT causes a downturn while $NbSe_2$ leads to an upturn of the magnetoresistance with the magnetic field increasing [see Figs. 2(c) and 2(g)].

With the whole heterostructure measurement configuration [see Fig. 2(i)], the temperature-dependent resistance shows two characteristic transitions at 23.7 and 7 K in Fig. 2(j), which correspond to the T_N of MBT and the T_c of $NbSe_2$, respectively. The magnetoresistance of the heterostructure in Fig. 2(k) reveals a downturn at 3.34 T following a nonlinear upturn transition at around 3 T, which can be related to the critical field of MBT (B_c^{MBT}) and $NbSe_2$ (B_c), respectively. On the other hand, the dV/dI-I curve of the heterostructure at 1.8 K [see Fig. 2(i)] demonstrates two pairs of transitions, locating at around ±895 and ± 245 μA, respectively, which will be discussed in detail in the following part.

The transport properties of the MBT/$NbSe_2$ interface were investigated by applying a current through two adjacent sides of the cross-shape heterostructure and measuring the voltage through the other two sides [see Fig. 2(m)]. The temperature

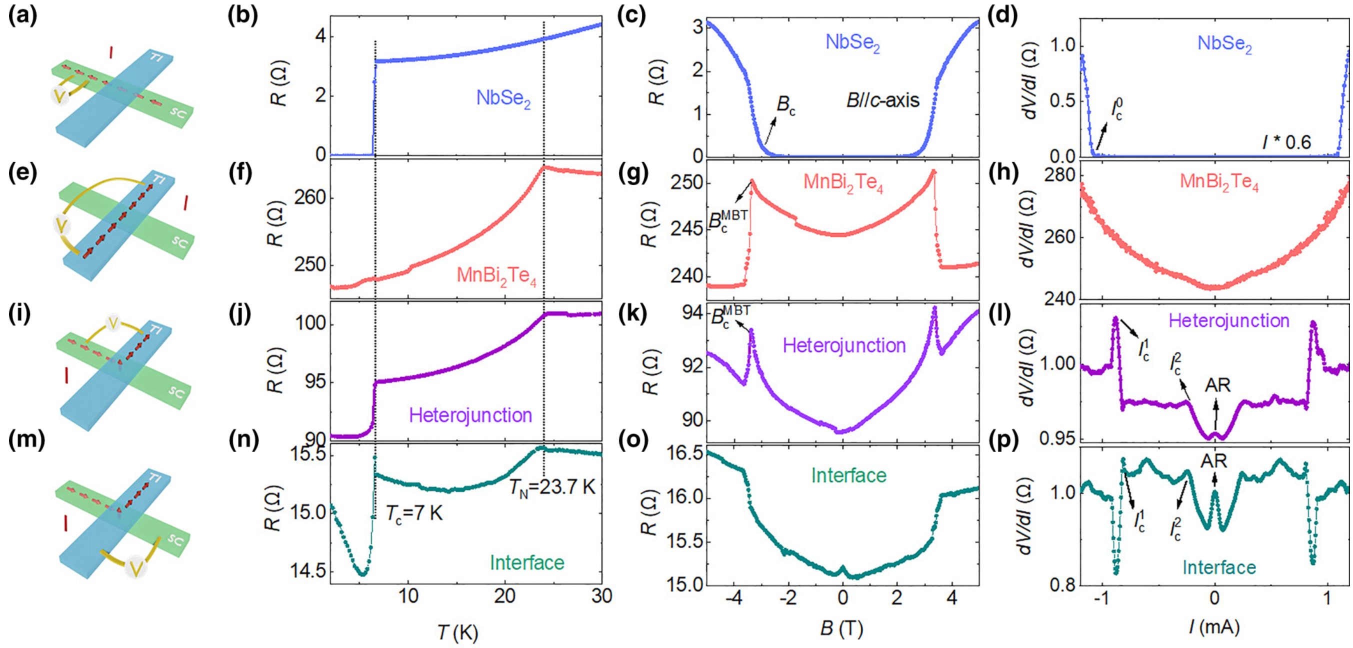

FIG. 2. Transport properties for different channels of the heterostructure. (a), (e), (i), and (m). Measurement schematic of the $NbSe_2$ (current 1-5, voltage 2-3 as shown in Fig. 1), MBT (6-9, 7-8), the whole heterostructure (1-6, 3-8), and the interface (1-6, 5-9) channels. (b), (f), (j), and (n). Temperature-dependent resistance for $NbSe_2$, MBT, MBT/$NbSe_2$ heterostructure, and interface, respectively. Here, all $R - T$ curves are measured under zero field. Particularly, two temperature transitions are identified at the R-T curve of the heterostructure and interface, including the superconducting transition Tc of $NbSe_2$ at 7 K and antiferromagnetic transition T_N of MBT at 23.7 K. The corresponding magnetoresistances at 1.8 K are given in (c), (g), (k), and (o), where the field was applied along the out-of-plane. The magnetic transition of MBT is observed in (g) and (k) as the spin-flop critical field (B_c^{MBT}), and the critical field of $NbSe_2$ exhibits in (c) as B_N. (d), (h), (l), and (p). The dV/dI vs I curves at 1.8 K for $NbSe_2$, MBT, MBT/$NbSe_2$ heterostructure, and the interface, respectively. Here, the current axis for $NbSe_2$ in (d) is timed 0.6, because the critical current of $NbSe_2$ is 1.8 mA.

dependence of resistance in Fig. 2(n) also shows two distinct transitions at 23.7 and 7 K, corresponding to the T_N and T_c, respectively. However, only an upturn transition is observed on the magnetoresistance curve as shown in Fig. 2(o), suggesting that the superconducting transition dominates the magnetoresistance at the interface. It is worth noting that the resistance of the interface exhibits an upturn behavior below the superconductivity transition, which can be attributed to the Andreev reflection (AR) effect. Such AR phenomenon also contributes to the peak of differential resistance at the zero-bias current as shown in Fig. 2(p). On the other hand, two pairs of transitions are observed at ±878 and ±248 μA on the dV/dI-I curve, which is consistent with those of heterostructure. However, these critical currents are significantly lower than that of the pristine $NbSe_2$, which is 1.8 mA at 1.8 K. These features can be attributed to the superconducting transitions of the reduced superconductivity at the surface of $NbSe_2$ and the proximity-effect-induced superconductivity at the surface of MBT [see Fig. 1(d)].

To understand the proximity-effect-induced superconductivity and AR effect through the heterostructure, we further studied the temperature-dependent dV/dI-I spectrums of the whole heterostructure and the interface. Figure 3(b) shows the mapping of normalized differential resistance at various temperatures of the whole heterostructure, and the differential resistances at some typical temperatures are given in Fig. 3(c). Three characteristic contour lines, labeled as I_c^0, I_c^1, and I_c^2, can be seen on both positive and negative current sides of the mapping in Fig. 3(b), corresponding to the peaks of the dV/dI-I curves shown in Fig. 3(c). It is worthy to mention that the temperature-dependent I_c^0, I_c^1, and I_c^2 and their corresponding gaps (Δ_0, Δ_1, and Δ_2) are consistent with the conventional BCS model as $\Delta_T = 1.74\Delta_0\sqrt{1 - T/T_c}$. Therefore, I_c^0, I_c^1, and I_c^2 can be attributed to the intrinsic $NbSe_2$, the reduced superconductivity at the surface of the $NbSe_2$, and the proximity-effect-induced superconductivity at the surface of the MBT.

In comparison, we perform the same measurement on the interface [see Fig. 3(d)]. The mapping results shown in Fig. 3(e) reveal the absence of I_c^0, which further confirms that I_c^0 corresponds to the intrinsic $NbSe_2$ since it is excluded during the measurement setup. Moreover, the transition of I_c^1 and I_c^2, and particularly the AR, are considerably more intense than those of the heterostructure. The main reason is that both $NbSe_2$ and MBT sides are excluded in this configuration, and the interfacial effect dominates the measurement result. Therefore, the cross-junction geometry is an ideal configuration to investigate the interfacial effects.

Considering the AR effect at an SC/non-SC interface, which is an effective method to determine the polarization P of a certain material [30,31], the reduction of the conductance at zero-bias current at the MBT/$NbSe_2$ interface indicates a weak spin-polarization from MBT. However, the MBT crystal in our case is about 40 nm thick

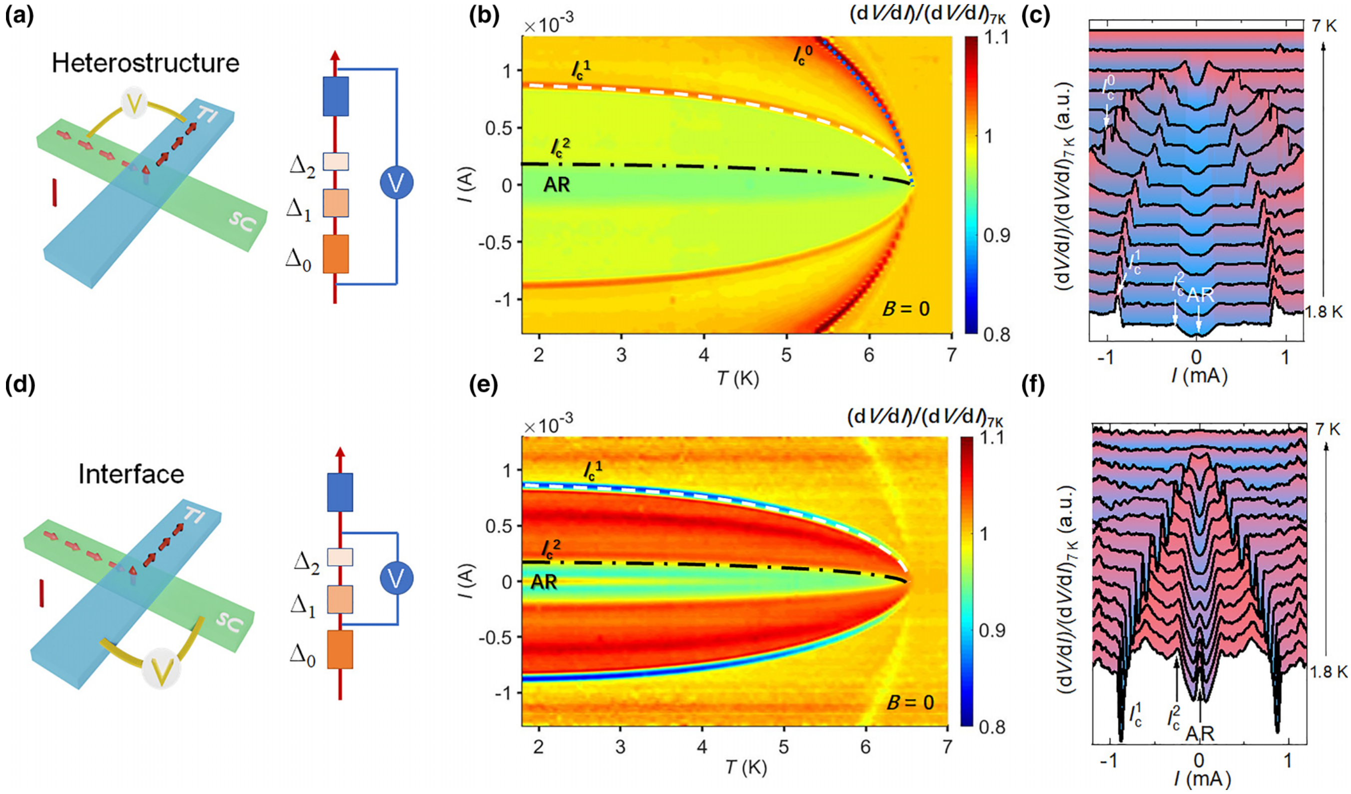

FIG. 3. Temperature-dependent critical current. Measurement schematic of (a) the whole MBT/$NbSe_2$ heterostructure and (d) the MBT/$NbSe_2$ interface. The differential resistance mapping of (b) the heterostructure and (e) the interface with the temperature ranging from 1.8 K to 7.0 K. The selected dV/dI-I spectrums of (c) the heterostructure and (f) the interface with several typical temperatures. I_c^0, I_c^1, and I_c^2 correspond to the critical currents of the intrinsic $NbSe_2$, the reduced superconductivity at the surface of the $NbSe_2$, and the proximity-effect-induced superconductivity at the surface of the MBT.

($\sim$10 SLs), which should demonstrate a long-term AFM coupling as a bulk crystal. For comparison, we also studied the AR behavior of the Fe_5GeTe_2/$NbSe_2$ heterostructure, where Fe_5GeTe_2 is a typical out-of-plane ferromagnet. Surprisingly, the dI/dV-V spectrums at the interface of MBT/$NbSe_2$ and Fe_5GeTe_2/$NbSe_2$ (see Fig. S5 [25]) are comparable. Therefore, we can conclude that the surface state of MBT reveals an FM ordering, which partially restricts the AR effect.

According to the temperature- and field-dependent dV/dI-I spectrums shown in Fig. 2 and Figs. S1–S3 of the Supplemental Material [25], we can confirm the observation of proximity-effect-induced superconductivity (Δ_2) at the surface of MBT. In principle, the AFM coupling and topological nontrivial state in the electron band structure may contribute to the superconducting coupling, resulting in a novel superconductivity gap symmetry or even topological superconductivity [32,33], which should be pronouncedly different from the conventional superconductivity in $NbSe_2$ [34–36]. To uncover the symmetry of the proximity-effect-induced superconductivity in MBT, we also measured the angular-dependent magnetoresistance spectrums of the whole MBT/$NbSe_2$ heterostructure and the interface.

The angular-dependent measurement geometry is shown in Fig. 4(b). Figures 4(a) and 4(c) show the mapping of angular-dependent dV/dI-I spectrums for the heterostructure and interface at 1.8 K under magnetic fields of 1, 4, and 9 T, respectively. In particular, the I_c^0, I_c^1, and I_c^2 are identified individually. Moreover, the extracted normalized critical currents $I_c/I_c^{0\mathrm{deg}}$ as a function of θ are plotted in Figs. 4(d) and 4(e), where θ is the angle between the magnetic field and a-axis direction of $NbSe_2$. Surprisingly, in contrast to what is generally considered as a conventional s-wave superconductor that should behave as an isotropic superconductivity symmetry, the angular-dependent I_c^0 reveals a cosine function with twofold symmetry, where the maximum appears at 0° and 180° and the minimum appears at 90° and 270°, respectively. According to the analysis by Hamill *et al.*, the spontaneous nematic superconductivity or the strong gap-mixing triggered by a small symmetry-breaking field may induce an anisotropic nature in finite layers of $NbSe_2$ [35], which is the probable origin of the twofold-symmetric I_c^0. However, a deeper understanding of the symmetry behavior is still needed.

The angular dependence of I_c^1 is comparable for both the heterostructure and the interface measurement configurations [see Figs. 4(d) and 4(e)]. Since I_c^1 comes from the reduced superconductivity at the surface of $NbSe_2$, it is not surprising that it has a cosine function with twofold symmetry. The phase of I_c^1 is slightly shifted compared to that of I_c^0, which is due to the influence of the MBT layer. Moreover, the proximity-effect-induced I_c^2 vanishes at a large field ($B = 9$ T) and roughly follows a cosine function with twofold symmetry as well at $B = 4$ T, indicating that an unconventional superconductivity is induced at the surface of MBT through the

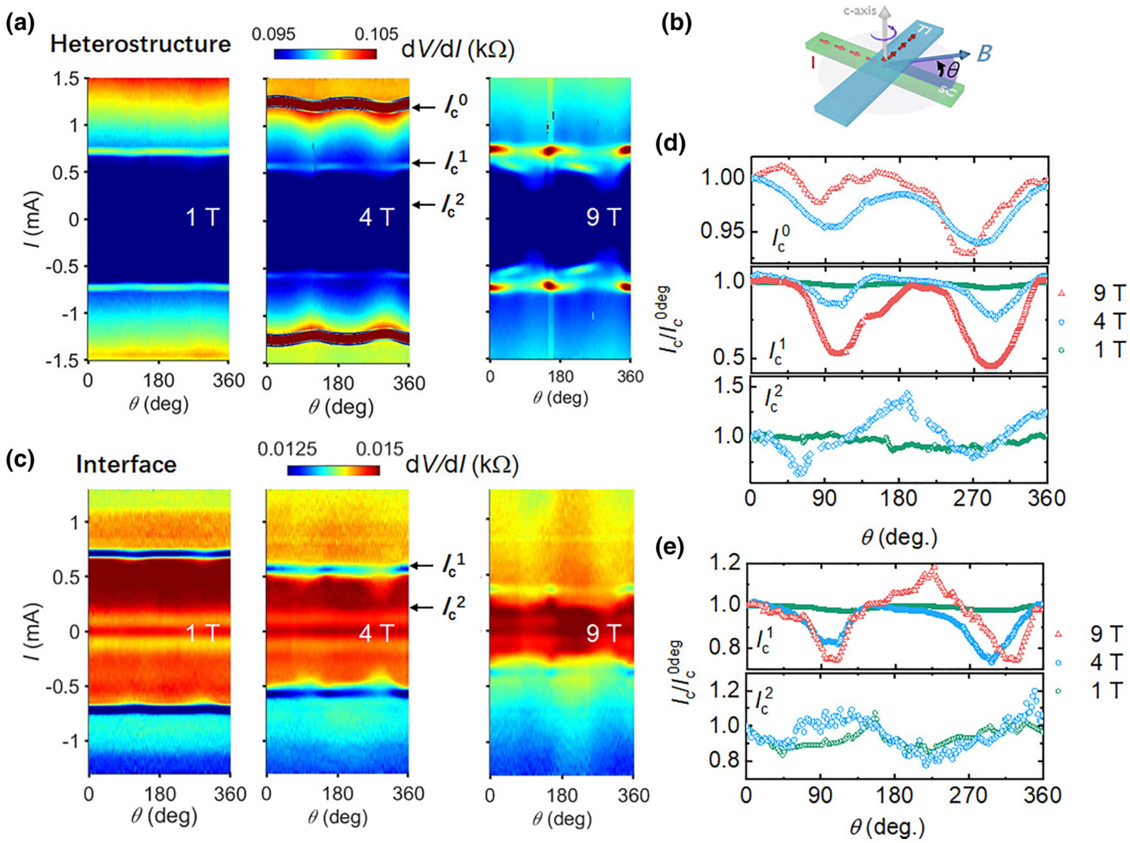

FIG. 4. Angular-dependent critical current at 1.8 K. (b) Schematic image of the measurement setup. Here, the magnetic field was applied within the in-plane, and θ corresponds to the angle between the current within the $NbSe_2$ and field B. (a) and (c). The angular-dependent differential resistance mapping under different magnetic fields for the whole heterostructure and the interface, respectively. (d) and (e). The angular-dependence of I_c^0, I_c^1, and I_c^2 at 4 T for the whole heterostructure and the interface, respectively. Here, I_c^0, I_c^1, and I_c^2 are estimated from mapping in (a) and (b).

proximity effect. In addition, the phase of I_c^2 is quite different from that of I_c^0 and I_c^1, because the phase of critical current only associates with the angle between the current and the long, straight edge of the SC flake [35], and I_c^2 and I_c^0 (I_c^1) come from the MBT layer and the $NbSe_2$ layer, respectively. Based on the angular-dependent profiles of I_c^0, I_c^1, and I_c^2, although we can hardly confirm the exact gap symmetry of the induced superconductivity at the surface of MBT, the superconductivity gap symmetry of Δ_2 are different from that of $NbSe_2$ (Δ_0), which is possibly due to the nontrivial topological nature or the magnetic ordering of the MBT.

In summary, we studied the van der Waals cross-shape heterostructure between a nontrivial TI MBT and a conventional SC $NbSe_2$. Through different measurement configurations, three different superconductivity gaps have been observed, including the intrinsic $NbSe_2$, the reduced superconductivity at the surface of the $NbSe_2$, and the proximity-effect-induced superconductivity at the surface of the MBT. A clear zero-bias peak was observed in the dV/dI-I curve that corresponds to the AR effect at an FM/SC interface, suggesting that the surface of MBT exhibits a ferromagnetically coupled plane. The temperature-, field- and angular-dependent dV/dI-I spectrums with the whole heterostructure and the interface measurement configurations have been systematically investigated. A twofold-symmetric superconductivity is observed at the surface of MBT, which has a different phase with an intrinsic few-layer $NbSe_2$. Although we cannot identify the superconductivity pairing symmetry, an unconventional superconducting state that is different from the intrinsic $NbSe_2$ should be seriously considered, as the various quantum states, such as topological states and magnetic ordering, may contribute to the electronic coupling.

This research was supported in part by the Ministry of Science and Technology (MOST) of China (No. 2022YFA1603903), the National Natural Science Foundation of China (Grants No. 12004251, No. 12104302, No. 12104303, and No. 12304217), the Science and Technology Commission of Shanghai Municipality, the Shanghai Sailing Program (Grant No. 21YF1429200), the start-up funding from ShanghaiTech University, Beijing National Laboratory for Condensed Matter Physics, the Interdisciplinary Program of Wuhan National High Magnetic Field Center (WHMFC202124), the open project from State Key Laboratory of Surface Physics and Department of Physics, Fudan University (Grant No. KF2022-13), the Shanghai Sailing Program (23YF1426900), the Double First-Class Initiative Fund of ShanghaiTech University, and the Science and Technology Commission of the Shanghai Municipality (21JC1405100). Growth of h-BN was supported by the Elemental Strategy Initiative conducted by the MEXT, Japan (JPMXP0112101001), JSPS KAKENHI (JP20H00354), and A3 Foresight by JSPS.

[1] S. M. Frolov, M. J. Manfra, and J. D. Sau, Nat. Phys. **16**, 718 (2020).

[2] M. Sato and Y. Ando, Rep. Prog. Phys. **80**, 076501 (2017).

[3] J. Clarke and F. K. Wilhelm, Nature (London) **453**, 1031 (2008).

[4] D. Zhu, T. Jaako, Q. He, and P. Rabl, Phys. Rev. Appl. **16**, 014024 (2021).

[5] D. A. Ivanov, Phys. Rev. Lett. **86**, 268 (2001).

[6] L. Fu and C. L. Kane, Phys. Rev. Lett. **100**, 096407 (2008).

[7] H.-H. Sun, K.-W. Zhang, L.-H. Hu, C. Li, G.-Y. Wang, H.-Y. Ma, Z.-A. Xu, C.-L. Gao, D.-D. Guan, Y.-Y. Li, C. Liu, D. Qian, Y. Zhou, L. Fu, S.-C. Li, F.-C. Zhang, and J.-F. Jia, Phys. Rev. Lett. **116**, 257003 (2016).

[8] R. M. Lutchyn, E. P. A. M. Bakkers, L. P. Kouwenhoven, P. Krogstrup, C. M. Marcus, and Y. Oreg, Nat. Rev. Mater. **3**, 52 (2018).

[9] H. Kim, A. Palacio-Morales, T. Posske, L. Rózsa, K. Palotás, L. Szunyogh, M. Thorwart, and R. Wiesendanger, Sci. Adv. **4**, eaar5251 (2018).

[10] V. Mourik, K. Zuo, S. M. Frolov, S. R. Plissard, E. P. A. M. Bakkers, and L. P. Kouwenhoven, Science **336**, 1003 (2012).

[11] S. Nadj-Perge, I. K. Drozdov, J. Li, H. Chen, S. Jeon, J. Seo, A. H. MacDonald, B. A. Bernevig, and A. Yazdani, Science **346**, 602 (2014).

[12] B. Jäck, Y. Xie, J. Li, S. Jeon, B. A. Bernevig, and A. Yazdani, Science **364**, 1255 (2019).

[13] Y. Liu, N. O. Weiss, X. Duan, H.-C. Cheng, Y. Huang, and X. Duan, Nat. Rev. Mater. **1**, 16042 (2016).

[14] A. K. Geim and I. V. Grigorieva, Nature (London) **499**, 419 (2013).

[15] D. Rhodes, S. H. Chae, R. Ribeiro-Palau, and J. Hone, Nat. Mater. **18**, 541 (2019).

[16] K. S. Novoselov, A. Mishchenko, A. Carvalho, and A. H. Castro Neto, Science **353**, aac9439 (2016).

[17] K. He, npj Quantum Mater. **5**, 90 (2020).

[18] C. Liu, Y. Wang, H. Li, Y. Wu, Y. Li, J. Li, K. He, Y. Xu, J. Zhang, and Y. Wang, Nat. Mater. **19**, 522 (2020).

[19] M. M. Otrokov, I. I. Klimovskikh, H. Bentmann, D. Estyunin, A. Zeugner, Z. S. Aliev, S. Gaß, A. U. B. Wolter, A. V. Koroleva, A. M. Shikin, M. Blanco-Rey, M. Hoffmann, I. P. Rusinov, A. Y. Vyazovskaya, S. V. Eremeev, Y. M. Koroteev, V. M. Kuznetsov, F. Freyse, J. Sánchez-Barriga, I. R. Amiraslanov *et al.*, Nature (London) **576**, 416 (2019).

[20] J. Li, Y. Li, S. Du, Z. Wang, B.-L. Gu, S.-C. Zhang, K. He, W. Duan, and Y. Xu, Sci. Adv. **5**, eaaw5685 (2019).

[21] Y. Deng, Y. Yu, M. Z. Shi, Z. Guo, Z. Xu, J. Wang, X. H. Chen, and Y. Zhang, Science **367**, 895 (2020).

[22] J. Chen, W. Xu, Z. Tan, Z. Pan, P. Zhu, Z.-M. Liao, and D. Yu, Nano Lett. **22**, 6484 (2022).

[23] W.-Z. Xu, C.-G. Chu, Z.-C. Pan, J.-J. Chen, A.-Q. Wang, Z.-B. Tan, P.-F. Zhu, X.-G. Ye, D.-P. Yu, and Z.-M. Liao, Phys. Rev. B **105**, 184515 (2022).

[24] A. I. Buzdin, Rev. Mod. Phys. **77**, 935 (2005).

[25] See Supplemental Material at http://link.aps.org/supplemental/10.1103/PhysRevB.109.L140503 for detailed methods of sample preparation and extended measurements of dV/dI-I spectrums with different conditions.

[26] H. F. Hess, R. B. Robinson, R. C. Dynes, J. M. Valles, and J. V. Waszczak, Phys. Rev. Lett. **62**, 214 (1989).

[27] A. Zeugner, F. Nietschke, A. U. B. Wolter, S. Gaß, R. C. Vidal, T. R. F. Peixoto, D. Pohl, C. Damm, A. Lubk, R. Hentrich, S. K. Moser, C. Fornari, C. H. Min, S. Schatz, K. Kißner, M. Ünzelmann, M. Kaiser, F. Scaravaggi, B. Rellinghaus, K. Nielsch *et al.*, Chem. Mater. **31**, 2795 (2019).

[28] J. Cui, M. Shi, H. Wang, F. Yu, T. Wu, X. Luo, J. Ying, and X. Chen, Phys. Rev. B **99**, 155125 (2019).

[29] S. H. Lee, Y. Zhu, Y. Wang, L. Miao, T. Pillsbury, H. Yi, S. Kempinger, J. Hu, C. A. Heikes, P. Quarterman, W. Ratcliff, J. A. Borchers, H. Zhang, X. Ke, D. Graf, N. Alem, C.-Z. Chang, N. Samarth, and Z. Mao, Phys. Rev. Res. **1**, 012011(R) (2019).

[30] R. J. Soulen, J. M. Byers, M. S. Osofsky, B. Nadgorny, T. Ambrose, S. F. Cheng, P. R. Broussard, C. T. Tanaka, J. Nowak, J. S. Moodera, A. Barry, and J. M. D. Coey, Science **282**, 85 (1998).

[31] G. J. Strijkers, Y. Ji, F. Y. Yang, C. L. Chien, and J. M. Byers, Phys. Rev. B **63**, 104510 (2001).

[32] K. E. Avers, W. J. Gannon, S. J. Kuhn, W. P. Halperin, J. Sauls, L. DeBeer-Schmitt, C. Dewhurst, J. Gavilano, G. Nagy, U. Gasser, and M. R. Eskildsen, Nat. Phys. **16**, 531 (2020).

[33] G. Du, Y. Li, J. Schneeloch, R. Zhong, G. Gu, H. Yang, H. Lin, and H.-H. Wen, Sci. China: Phys. Mech. Astron. **60**, 037411 (2017).

[34] X. Xi, Z. Wang, W. Zhao, J.-H. Park, K. T. Law, H. Berger, L. Forró, J. Shan, and K. F. Mak, Nat. Phys. **12**, 139 (2016).

[35] A. Hamill, B. Heischmidt, E. Sohn, D. Shaffer, K.-T. Tsai, X. Zhang, X. Xi, A. Suslov, H. Berger, L. Forró, F. J. Burnell, J. Shan, K. F. Mak, R. M. Fernandes, K. Wang, and V. S. Pribiag, Nat. Phys. **17**, 949 (2021).

[36] T. Yokoya, T. Kiss, A. Chainani, S. Shin, M. Nohara, and H. Takagi, Science **294**, 2518 (2001).